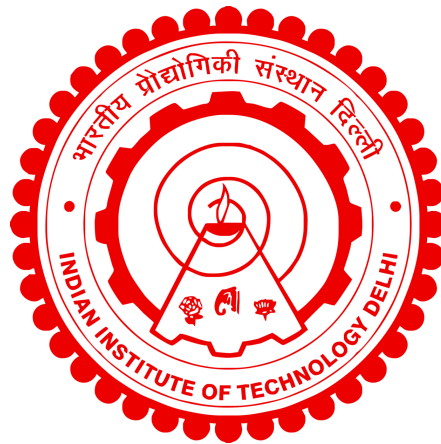


**FIBER-INTEGRATED  
PPLN-WAVEGUIDE-BASED QUANTUM LIGHT  
SOURCES FOR LOW-QBER QUANTUM  
COMMUNICATION AND SENSING  
APPLICATIONS**

**AKANKSHA ANGURAL**



**DEPARTMENT OF PHYSICS  
INDIAN INSTITUTE OF TECHNOLOGY DELHI**

**April 2026**

© Indian Institute of Technology Delhi (IITD), New Delhi, 2026

**Fiber-integrated PPLN-waveguide-based quantum  
light sources for Low-QBER quantum communication  
and sensing applications**

*by*

**AKANKSHA ANGURAL**

Department of Physics

*Submitted*

*in fulfillment of the requirements of the degree of*

**Doctor of Philosophy**

*to the*



**INDIAN INSTITUTE OF TECHNOLOGY DELHI**

**April 2026**

*Dedicated to my family...*

# Certificate

---

This is to certify that the thesis entitled “**Fiber-integrated PPLN-waveguide-based quantum light sources for Low-QBER quantum communication and sensing applications**”, submitted by **Akanksha Angural** to the Indian Institute of Technology Delhi, for the award of the degree of **Doctor of Philosophy** in Physics, is a record of the original, bonafide research work carried out by her under my supervision and guidance. The thesis has reached the standards that meet the requirements of the regulations related to the award of the degree.

The results contained in this thesis have not been submitted in part or in full to any other University or Institute for the award of any degree or diploma to the best of my knowledge.

**Prof. Joyee Ghosh**

Associate Professor, Department of Physics

Indian Institute of Technology Delhi

New Delhi, 110016

Date: April 13, 2026

# Acknowledgements

I want to express my heartfelt gratitude to everyone who supported me in my Ph.D. journey. This thesis is a culmination of not only of my own efforts but also of the guidance, encouragement, and kindness I have received from many individuals over the years.

First and foremost, I would like to express my deepest and most sincere gratitude to my supervisor, **Prof. Joyee Ghosh**, for her exceptional mentorship and unwavering support throughout the course of my doctoral research. Her scientific insights, patience, and continuous encouragement have been invaluable to me. She has always inspired me to think critically, to aim higher, and to approach challenges with both curiosity and depth. The freedom she provided me to explore my ideas, balanced with her thoughtful guidance and constructive feedback, has shaped my growth as a researcher in ways I will always cherish. I am truly grateful for her trust, her time, and her ability to make even the most complex discussions feel approachable and enriching. I truly believe that she has been like the wind beneath my wings, enabling me to rise through challenges and reach heights I could not have imagined on my own.

I am also grateful to my research committee members, **Prof. R. K. Varshney**, **Prof. Joby Joseph**, and **Prof. Abhishek Dixit**, for their constructive feedback and helpful suggestions during the SRC review meetings, which significantly enriched the quality of this work.

I also acknowledge **DST India** for the project grant (DST/ICPS/QuST/Theme-1/2019/Q-62) and my fellowship and **IIT Delhi** for the RSTA travel grant, and the Department of Physics and its non-teaching staff for their continuous support.

I am deeply grateful to **Dr. Terry McRae** and **Dr. Jiayi Qin**, under whom I undertook a research project at the Australian National University. Their guidance and insightful discussions during my stay broadened my perspective, strengthened my understanding of the field and has been truly intellectually rewarding.

I would also like to express my heartfelt thanks to all my lab members, **Dr. Ramesh Kumar**, **Dr. Vineet Kumar Shukla**, **Dr. Shivani Sharma**, **Dr. Omshankar**, **Dr. Rajni**, **Dr. Vikash Kumar Yadav**, **Bharti**, **Vijay**, **Nilesh**, **Khushboo**, **Gourav**, **Shibam**, **Abhishek** and **Priya**, for creating a collaborative yet light environment in

the lab. Their readiness to help at any moment whether during long experimental days, troubleshooting stubborn setups, or discussing new ideas created an environment of collaboration and support that I deeply appreciate. Among them, Bharti has been the friend without whom I cannot imagine this journey. The many hours we spent together in the lab or drinking coffee, the shared frustrations when experiments failed, and the collective excitement when things finally worked made this journey far more enjoyable and memorable. I am also especially grateful to Dr. Omshankar and Dr. Vikash for their readiness to engage in long and meaningful discussions, their readiness to help with different aspects of the experiments, and their genuine involvement in refining setups, troubleshooting issues, and interpreting results have been invaluable to me. Dr. Shivani and Vijay have also contributed immensely through their constant camaraderie and the warmth. Our casual conversations, discussions about the future, and everyday interactions provided a sense of ease and positivity to my time in the lab.

My profound gratitude also goes to my **family**, who have been my strongest pillars of support. My parents' encouragement and constant emotional support gave me resilience, and my brother's motivation and willingness to help whenever I needed it made this journey smoother. I am equally thankful to my husband, whose patience, understanding, and unwavering support gave me strength throughout this journey. I am truly blessed to have him by my side. To my friends outside the lab, I extend my warmest thanks for the comfort, laughter, long talks and companionship that made the most difficult days easier to endure.

Finally, I would like to acknowledge everyone who, in one way or another, contributed to my academic and personal development. Each interaction, piece of advice, and gesture of support has helped shape this thesis and the person I have become through this process. This work stands as much on their contributions as it does on my own efforts.

# Abstract

The generation, characterization, and application of non-classical states of light is fundamental to state-of-the-art quantum communication and sensing technologies. This thesis focuses on the development and performance optimization of fiber-integrated, periodically poled lithium niobate (ppLN) ridge-waveguide-based quantum light sources tailored for both discrete-variable (DV) and continuous-variable (CV) applications. These sources are intended for real-time implementation in secure quantum communication and sensing systems. All sources developed in this work are realized using single pass spontaneous parametric down-conversion (SPDC) in magnesium-oxide-doped periodically poled lithium niobate (MgO:ppLN) ridge waveguides. We first systematically explore type-II quasi-phase-matched MgO:ppLN waveguide for DV characterization, enabling the generation of narrowband, spectral and polarization-correlated biphotons at 1560 nm with high spectral brightness ( $\sim 5 \times 10^6$  pairs/s/mW/nm), coincidence-to-accidental ratio ( $\sim 427$ ) and comparatively narrow emission bandwidth ( $\sim 2.4$  nm) along with strong spectral correlations revealed by joint spectral intensity measurements. Since type-II SPDC generates orthogonally polarized photons, temporal distinguishability may arise due to anisotropy and fiber-integration of the source. Hence, subsequent investigations address how detection system parameters, including single-photon detector quantum efficiency, dead time, and time-correlator bin width impact the measured photon statistics and temporal quantum correlations. While introducing birefringence compensation. Analytical modeling and experimental validation demonstrate that optimized detection conditions can yield exceptionally high temporal cross-correlations ( $g_{si}^{(2)}(0) \sim 10^4$ ) and near-unity raw Hong-Ou-Mandel interference visibilities ( $\sim 99 \pm 1\%$ ), demonstrating the intrinsic indistinguishability and quality of the generated photon pairs. Building on this foundation, we further present the realization of a robust, fiber-integrated polarization-entangled photon-pair source. One highlight of this thesis is that using the same system and setup, this source is capable of generating both bosonic ( $|\psi^+\rangle$ ) and fermionic ( $|\psi^-\rangle$ ) Bell states. This is achieved by controlling the phase symmetry between the two arms after splitting the photon pairs, rendering the source switchable between the two states. The generated entangled states exhibit high raw concurrence ( $> 92\%$ ), raw fidelity ( $> 95\%$ ), and low QBER ( $< 3\%$ ), with strong violation of the CHSH inequality ( $S > 2.65$ ), confirming their potential for secure quantum key distribution and quantum networking. We further extend the scope of this thesis to the generation and characterization of quantum squeezed states in

the telecom C-band using a fully guided MgO:ppLN waveguide-based source presenting the first indigenous waveguide squeezer at telecom wavelengths. Theoretical analyses of balanced homodyne detection (BHD) circuits are performed for two configurations- a current subtraction design with a differential fine tuning circuit and adjustable bias voltage, and a variable gain design with an additional differential amplifier. This enables a study of the best configuration for enhanced transimpedance gain, high bandwidth and low electronic noise, which can thereby be employed for improving squeezed-state detection sensitivity. Utilizing this BHD circuit, an operational study of fully-guided single-mode squeezing in the telecom C-band is done using a Zn-indiffused MgO:ppLN ridge waveguide (using type-0 SPDC), achieving  $-1.81 \pm 0.05$  dB of measured squeezing (corresponding to  $-4.11 \pm 0.05$  dB of generated squeezing), notably using off-the-shelf components. The quantum utility of the source under real-time noise constraints is investigated and quantified through a computation of the purity, Von-Neumann entropy and quantum Fisher information, showing enhancement in phase sensing. Additionally, entanglement potential, Duan's inseparability criterion and quantum teleportation fidelity are also computed. All these parameters, establish quantitative benchmarks for evaluating the performance of such guided-wave sources. Overall, this work demonstrates fiber-integrated waveguide-based sources as compact, stable, and scalable building blocks capable for quantum communication, metrology, and sensing applications in practical telecom environments for both DV and CV classifications.

## सार

प्रकाश की नॉन-क्लासिकल अवस्थाओं का सृजन, विशेषण तथा अनुप्रयोग आधुनिक क्वांटम संचार और संवेदन प्रौद्योगिकियों की एक मूलभूत आवश्यकता है। यह शोधप्रबंध फाइबर-समेकित, आवधिक रूप से ध्रुवीकृत लिथियम नायोबेट (पीपीएलएन) रिज-तरंगमार्ग आधारित क्वांटम प्रकाश स्रोतों के विकास और प्रदर्शन के अनुकूलन पर केंद्रित है, जिन्हें डिस्क्रीट-वेरिएबल (डीवी) तथा कंटिन्यूअस-वेरिएबल (सीवी) दोनों अनुप्रयोगों के लिए तैयार किया गया है। ये स्रोत सुरक्षित क्वांटम संचार और संवेदन प्रणालियों में वास्तविक समय कार्यान्वयन के लिए अभिकल्पित हैं। इस कार्य में विकसित सभी स्रोत मैग्नीशियम-ऑक्साइड-मिश्रित आवधिक ध्रुवीकृत लिथियम नायोबेट (एमजीओ:पीपीएलएन) रिज-तरंगमार्गों में एकल-पास स्वस्फूर्त पैरामीट्रिक डाउन-परिवर्तन (एसपीडीसी) के माध्यम से साकार किए गए हैं। सर्वप्रथम डीवी विशेषण हेतु टाइप-द्वितीय अर्ध-फेज-सामंजस्यित एमजीओ:पीपीएलएन तरंगमार्ग का व्यवस्थित अध्ययन किया गया, जिससे 1560 नैनोमीटर पर संकीर्ण-वर्णक्रमीय, वर्णक्रम तथा ध्रुवण-सहसंबद्ध द्वि-फोटॉनों का सृजन संभव होता है। इनकी उच्च वर्णक्रमीय दीप्ति  $\sim 5 \times 10^6$  युग्म/सेकंड/मिलिवाट/नैनोमीटर, सह-घटना से आकस्मिक अनुपात ( $\sim 427$ ) तथा तुलनात्मक रूप से संकीर्ण उत्सर्जन वर्णपट्टी चौड़ाई ( $\sim 2.4$  नैनोमीटर) प्राप्त हुई, साथ ही संयुक्त वर्णक्रमीय तीव्रता मापन से प्रबल वर्णक्रमीय सहसंबंध भी प्रकट हुए। चूँकि टाइप-द्वितीय एसपीडीसी परस्पर लम्बवत ध्रुवीकृत फोटॉन उत्पन्न करता है, अतः स्रोत की दिशात्मक असमानता और फाइबर-समेकन के कारण समयगत पृथकता उत्पन्न हो सकती है। इसलिए आगे के अध्ययन यह दर्शाते हैं कि डिटेक्शन तंत्र के पैरामीटर — जैसे एकल-फोटॉन डिटेक्टर की क्वांटम दक्षता, निष्क्रिय समय और समय-सहसंबंधक की बिन चौड़ाई मापी गई फोटॉन सांख्यिकी तथा समयगत क्वांटम सहसंबंधों को किस प्रकार प्रभावित करते हैं, साथ ही द्विविचलन क्षतिपूर्ति भी प्रस्तुत की गई है। विश्लेषणात्मक मॉडलन और प्रयोगात्मक प्रमाणीकरण से यह प्रदर्शित होता है कि अनुकूलित डिटेक्शन परिस्थितियों में अत्यंत उच्च समयगत पार-सहसंबंध ( $g_{si}^{(2)}(0) \sim 10^4$ ) तथा लगभग एकात्मक हांग-ऊ-मैंडल व्यतिकरण दृश्यता ( $99 \pm 1\%$ ) प्राप्त होती है, जो उत्पन्न फोटॉन युग्मों की अंतर्निहित अविभेद्यता और उच्च गुणवत्ता को प्रमाणित करती है। इसी आधार पर एक सुदृढ़, फाइबर-समेकित, ध्रुवण-संयोजित फोटॉन-युग्म स्रोत का साकार प्रस्तुत किया गया है। इस शोध की प्रमुख विशेषता यह है कि समान प्रणाली और सेटअप से यह स्रोत दोनों बोसोनिक ( $|\psi^+\rangle$ ) तथा फर्मियोनिक ( $|\psi^-\rangle$ ) बेल अवस्थाएँ उत्पन्न कर सकता है। यह फोटॉन युग्मों के विभाजन के पश्चात दोनों भुजाओं के मध्य चरण सममिति को नियंत्रित कर प्राप्त किया गया है, जिससे स्रोत को दोनों अवस्थाओं के बीच स्विच योग्य बनाया जा सकता है। उत्पन्न संयोजित अवस्थाएँ उच्च कच्ची सहसम्बद्धता ( $> 92\%$ ), उच्च कच्ची विशुद्धता ( $> 95\%$ ) तथा निम्न क्यूबीईआर ( $< 3\%$ ) प्रदर्शित करती हैं। साथ ही सीएचएसएच असमानता का प्रबल उल्लंघन ( $S > 2.65$ ) इनके सुरक्षित क्वांटम कुंजी वितरण और क्वांटम नेटवर्किंग में उपयोग की पुष्टि करता है। इस शोध का विस्तार आगे दूरसंचार सी-बैंड में क्वांटम संपीडित अवस्थाओं के सृजन और विशेषण तक किया गया, जिसके लिए एक पूर्णतः निर्देशित एमजीओ:पीपीएलएन तरंगमार्ग आधारित स्रोत का उपयोग किया गया, जो दूरसंचार तरंगदैर्घ्य पर प्रथम स्वदेशी तरंगमार्ग संपीडक प्रस्तुत करता है। संतुलित होमोडाइन अभिज्ञापन परिपथों का सैद्धांतिक विश्लेषण दो विन्यासों हेतु किया गया - (1) धारा-घटाव आधारित विन्यास, जिसमें विभेदक सूक्ष्म-संयोजन परिपथ और समायोज्य बायस वोल्टेज सम्मिलित हैं, (2) परिवर्ती प्रवर्धन आधारित विन्यास, जिसमें अतिरिक्त विभेदक प्रवर्धक जोड़ा गया है। इससे सर्वोत्तम विन्यास का निर्धारण संभव हुआ, जो उच्च ट्रांसइम्पीडेंस प्रवर्धन, अधिक बैंडचौड़ाई और न्यून इलेक्ट्रॉनिक शोर प्रदान करता है, जिससे संपीडित अवस्था पहचान संवेदनशीलता

में वृद्धि की जा सके। इस परिपथ का उपयोग करते हुए दूरसंचार सी-बैंड में पूर्णतः निर्देशित एकल-मोड संपीडन का अध्ययन जिंक-प्रसारित एमजीओ:पीपीएलएन रिज-तरंगमार्ग में किया गया, जिसमें  $-1.81 \pm 0.05$  डेसीबेल का मापा गया संपीडन प्राप्त हुआ, जो  $-4.11 \pm 0.05$  डेसीबेल उत्पन्न संपीडन के अनुरूप है, और यह सब मानक व्यावसायिक अवयवों के प्रयोग से संभव हुआ। वास्तविक समय शोर प्रतिबंधों के अंतर्गत स्रोत की क्वांटम उपयोगिता का मूल्यांकन शुद्धता, वॉन-न्यूमैन एंट्रॉपी तथा क्वांटम फिशर सूचना के माध्यम से किया गया, जिससे चरण संवेदन में उन्नति प्रदर्शित हुई। इसके अतिरिक्त संयोजन संभाव्यता, डुआन की अविभाज्यता कसौटी तथा क्वांटम टेलीपोर्टेशन विश्वसनीयता की भी गणना की गई। ये सभी पैरामीटर ऐसे निर्देशित-तरंग स्रोतों के प्रदर्शन मूल्यांकन हेतु मात्रात्मक मानक स्थापित करते हैं। समग्र रूप से यह कार्य फाइबर-समेकित तरंगमार्ग आधारित स्रोतों को संक्षिप्त, स्थिर और स्केलेबल क्वांटम निर्माणखंड के रूप में स्थापित करता है, जो व्यावहारिक दूरसंचार परिवेश में डीवी तथा सीवी दोनों वर्गीकरणों हेतु क्वांटम संचार, मापन तकनीक और संवेदन अनुप्रयोगों में सक्षम सिद्ध होते हैं।

# Contents

Certificate

Acknowledgements

Abstract

Contents

List of Figures

List of Tables

Abbreviations

Symbols

<b>1</b>	<b>Introduction</b>	<b>1</b>
1.1	Origin of nonclassical state generation . . . . .	5
1.1.1	Maxwell's equations and the wave equation . . . . .	6
1.1.2	Frequency mixing and the origin of new frequency components . . . . .	8
1.2	Second-harmonic generation . . . . .	8
1.3	Phase-matching techniques . . . . .	11
1.3.1	Birefringent Phase Matching (BPM) . . . . .	12
1.3.2	Quasi-phase matching (QPM) . . . . .	14
1.4	Spontaneous parametric down-conversion . . . . .	15
1.4.1	Types of SPDC interactions . . . . .	18
1.4.2	Collinear and Non-Collinear SPDC . . . . .	19
1.4.3	Degenerate and non-degenerate SPDC . . . . .	20
1.5	Discrete-variable regime . . . . .	20
1.5.1	Detection . . . . .	20

1.5.2	Source characterization . . . . .	22
1.5.2.1	Spectral brightness . . . . .	22
1.5.2.2	SPDC conversion efficiency . . . . .	23
1.5.2.3	Coincidence-to-accidentals ratio (CAR) . . . . .	24
1.5.2.4	Coincidence-to-signal ratio (CSR) . . . . .	25
1.5.2.5	Joint spectral intensity (JSI) measurements . . . . .	26
1.5.3	Quantum entanglement . . . . .	27
1.5.3.1	Hong–Ou–Mandel interference and photon indistinguishability . . . . .	28
1.5.3.2	Two-Photon interference in orthogonal polarization bases . . . . .	31
1.5.3.3	CHSH-Bell parameter . . . . .	33
1.5.3.4	Quantum bit error rate (QBER) . . . . .	34
1.5.3.5	Quantum state tomography . . . . .	35
1.6	Continuous-variable regime . . . . .	37
1.6.1	Squeezed states . . . . .	38
1.6.2	Detection methods . . . . .	40
1.6.2.1	Homodyne detection . . . . .	40
1.6.3	Experimental characterization . . . . .	43
1.6.4	Evaluating the quantum utility of generated squeezed states . . . . .	44
1.7	Thesis layout . . . . .	45
<b>2</b>	<b>MgO:ppLN waveguide: Modal characterization and frequency-doubling</b>	<b>47</b>
2.1	Introduction . . . . .	48
2.2	Lithium Niobate as a Nonlinear Optical Material . . . . .	49
2.2.1	Doping the material . . . . .	50
2.3	Advantages of fiber-integrated waveguide platforms . . . . .	51
2.4	Waveguide design and fabrication . . . . .	51
2.4.1	Type-II MgO:ppLN ridge waveguide . . . . .	52
2.4.2	Type-0 Zn-Indiffused MgO:ppLN Waveguide . . . . .	53
2.5	Frequency doubling and phase-matching characterization . . . . .	54
2.5.1	Modal analysis and theoretical phase-matching verification . . . . .	54
2.5.2	Experimental Setup and SHG Characterization . . . . .	56
2.6	Summary . . . . .	59
<b>3</b>	<b>Development and characterization of a narrowband type-II SPDC-based waveguide source at 1560nm</b>	<b>61</b>
3.1	Introduction . . . . .	62
3.2	Experimental Setup for SPDC characterization . . . . .	63
3.3	Results and discussion . . . . .	65
3.3.1	Temperature-dependence of SPDC . . . . .	65
3.3.1.1	Spectral Brightness Calculation . . . . .	67
3.3.1.2	SPDC conversion efficiency . . . . .	68

3.3.2	Pump-power dependence of SPDC . . . . .	70
3.3.2.1	Singles and Coincidence count rates . . . . .	70
3.3.2.2	Coincidence-to-accidental ratio (CAR) . . . . .	71
3.3.2.3	Coincidence-to-signal ratio (CSR) . . . . .	72
3.3.3	Joint spectral intensity (JSI) measurements . . . . .	73
3.4	Summary . . . . .	77
<b>4</b>	<b>Optimizing quantum correlation measurements by manipulating detection parameters and application in Hong-Ou-Mandel interferometry</b>	<b>79</b>
4.1	Introduction . . . . .	81
4.2	Modeling the detection and correlation parameters . . . . .	82
4.2.1	Quantum efficiency ( $\eta$ ) . . . . .	83
4.2.2	Dead time ( $\tau_d$ ) . . . . .	84
4.2.3	Bin width ( $\tau_{bw}$ ) . . . . .	86
4.3	Second-order cross-correlations ( $g_{si}^{(2)}(0)$ ) . . . . .	88
4.4	Experimental setup . . . . .	90
4.5	Results and discussion . . . . .	92
4.5.1	Effect of quantum efficiency . . . . .	93
4.5.2	Effect of dead time . . . . .	94
4.5.3	Effect of bin width . . . . .	97
4.6	Application in HOM interferometry . . . . .	99
4.7	Summary . . . . .	103
<b>5</b>	<b>Fiber-integrated generation of high-fidelity tunable polarization-entangled states for low-QBER quantum applications</b>	<b>105</b>
5.1	Introduction . . . . .	107
5.2	Experimental Setup . . . . .	108
5.2.1	Classical optimization of polarizers . . . . .	110
5.3	Results and Discussion . . . . .	112
5.3.1	Bosonic and fermionic state manipulation . . . . .	112
5.3.2	Two-photon interference in orthogonal bases . . . . .	114
5.3.3	CHSH–Bell inequality measurements . . . . .	115
5.3.4	Quantum bit error rate (QBER) . . . . .	116
5.3.5	Entanglement mapping via quantum state tomography . . . . .	117
5.3.6	Temporal stability of entanglement metrics . . . . .	118
5.3.7	Impact of pump power on entanglement quality . . . . .	119
5.4	Summary . . . . .	122
<b>6</b>	<b>Homodyne detection circuit architectures for precision squeezing measurements</b>	<b>123</b>
6.1	Introduction . . . . .	124
6.2	Methods Used for Circuit Characterization . . . . .	125

6.2.1	AC (Steady-State) Analysis . . . . .	126
6.2.1.1	Bode Plots and Stability Assessment . . . . .	126
6.2.2	Transient Analysis . . . . .	128
6.2.3	Noise Analysis . . . . .	129
6.3	Circuit analysis for different BHD designs . . . . .	130
6.3.1	Current-subtraction configuration . . . . .	130
6.3.1.1	Adjustable bias voltage (ABV) . . . . .	131
6.3.1.2	Differential fine-tuning circuit . . . . .	133
6.3.1.3	Performance of the current-subtraction design . . . . .	133
6.3.2	Variable-gain configuration . . . . .	135
6.3.2.1	Noise reduction using differential amplifiers . . . . .	137
6.4	Common mode rejection ratio measurements in BHD . . . . .	138
6.5	Summary . . . . .	140
<b>7</b>	<b>Fully guided single mode squeezing: quantum advantage for quantum sensing and teleportation</b> . . . . .	<b>141</b>
7.1	Introduction . . . . .	142
7.2	Experimental setup . . . . .	144
7.3	Results and discussion . . . . .	147
7.3.1	Efficiency budget and loss analysis . . . . .	148
7.4	Evaluating the quantum utility of the squeezer . . . . .	150
7.4.1	State Purity and Entropy . . . . .	150
7.4.2	Quantum Fisher information and phase sensitivity . . . . .	153
7.4.3	Entanglement potential of the squeezed thermal state . . . . .	155
7.4.4	Establishing nonclassicality via Duan's inseparability criterion . . . . .	156
7.4.5	Quantum teleportation fidelity . . . . .	158
7.5	Summary . . . . .	162
<b>8</b>	<b>Conclusion and Future Scope</b> . . . . .	<b>163</b>
8.1	Future scope of this work: . . . . .	169
	<b>Appendix A: Balanced Homodyne Detection Circuitry</b> . . . . .	<b>175</b>
	<b>Bibliography</b> . . . . .	<b>179</b>
	<b>List of Publications</b> . . . . .	<b>201</b>
	<b>Biography</b> . . . . .	<b>207</b>

# List of Figures

1.1	Schematic of second harmonic generation (SHG) process using a non-centrosymmetric ( $\chi^{(2)} \neq 0$ ) optical medium under the conditions of energy and momentum conservation. . . . .	9
1.2	Comparison of generated field amplitude versus propagation length for optical nonlinear processes under (i) perfect phase-matching ( $\Delta k = 0$ ), (ii) quasi-phase-matching ( $\Delta k = k_{\text{QPM}}$ ), (iii) birefringent phase-matching ( $\Delta k = k_{\text{BPM}}$ ), and (iv) no phase-matching ( $\Delta k \neq 0$ ) [66]. . . . .	12
1.3	Birefringent phase-matching (type-I) for a negative crystal. . . . .	13
1.4	Periodic poling in a nonlinear optical media to achieve quasi-phase-matching. . . . .	14
1.5	Schematic for spontaneous parametric down-conversion (SPDC) process using a periodically poled $\chi^{(2)} \neq 0$ medium under the conditions of energy and momentum conservation to generate discrete and continuous variable modes. . . . .	15
1.6	Collinear and Non-collinear generation and propagation of signal and idler photons. . . . .	19
1.7	Typical bi-directional histogram observed during DV quantum measurements with peak representing the detected coincidences and base representing the accidental coincidences. . . . .	25
1.8	(a)Two-photon interference at 50:50 beam splitter leading to either (b) a dip due to bosonic symmetry or (c) a peak due to fermionic symmetry. . . . .	28
1.9	Two-photon interference in mutually orthogonal bases for $ \psi^-\rangle$ Bell state. . . . .	32
1.10	Simplified polarization analyzer setup for quantum state projection. . . . .	32
1.11	Reconstructed density matrices with real and imaginary parts showing 100% (ideal) fidelity for $ \psi^+\rangle$ and $ \psi^-\rangle$ Bell states. . . . .	37
1.12	Quadrature components and quantum vacuum squeezing depicting reduced quantum noise in phase quadrature and anti-squeezing in amplitude quadrature. . . . .	38
1.13	Balanced homodyne detection schematic depicting optical mixing of squeezed signal and local oscillator (LO) at a 50:50 beam splitter and further detection and subtraction to extract measurable squeezing. . . . .	40
1.14	Typical squeezing curve showing noise power spectral density with time as LO phase changes simulated in <i>Finesse 2</i> software [107]. . . . .	43
2.1	Image of type-II fiber-pigtailed waveguide source. . . . .	52

2.2	Image of type-0 fiber-pigtailed waveguide source. . . . .	53
2.3	Type-II waveguide, (a) cross-section and dimensions and (b) refractive index (RI) profile of the channel. . . . .	55
2.4	Waveguide modal simulations showing well-confined, (a) TE-like modes at 780 nm, (b) TE-like, and (c) TM-like modes at 1560 nm. . . . .	56
2.5	Schematic of the experimental setup for frequency doubling in the fiber-pigtailed type-II MgO:ppLN ridge waveguide. The pump at 1560 nm is coupled into the input fiber, polarization-controlled, and frequency-doubled in the waveguide to generate 780 nm light. The output is separated using a dichroic mirror, and the SHG power is measured as a function of temperature and pump wavelength. . . . .	57
2.6	Second-harmonic generation (SHG) performance of the waveguide, (a) temperature-dependent SHG efficiency, (b) SHG tuning with pump wavelength, (c) SHG power scaling quadratically with pump power, and (d) linear dependence of phase-matching wavelength on temperature. Theory curves show good agreement with experimental data. . . . .	58
3.1	Schematic for generation of correlated photon-pairs using fully-guided type-II SPDC waveguide-based source. Key components include: polarization controller (PC), in-line optical filter (IOF), digital tunable filter (DTF), fiber polarization beam splitter (FPBS), and single photon detector (SPD). . . . .	64
3.2	(a) Normalized signal (H) and idler (V) single-photon count rates as a function of waveguide temperature, (b) coincidence counts over 10 s, highlighting the optimal temperature region where spectral overlap and phase-matching efficiency are maximized. . . . .	66
3.3	Pump-power dependence of the generated photon pairs. (a) Signal counts increase with pump power and approach saturation at higher powers > 2 mW; inset shows the response on a log-scale pump axis. (b) Coincidence counts (per 10 s) showing similar saturation behaviour; inset presents the log-scale dependence. These measurements characterize the source brightness and pump-power scaling of the SPDC process. . . . .	70
3.4	Coincidence-to-accidental ratio (CAR) as a function of pump power, demonstrating the balance between increasing pair-generation rate and pump-induced background noise. . . . .	72
3.5	Coincidence-to-single ratio (CSR) plotted as a function of pump power. . . . .	73
3.6	Schematic for JSI measurements using two digital tunable filters, one in each arm, allowing independent spectral selection of the signal and idler photons before coincidence analysis. . . . .	75
3.7	(a) Normalized coincidence counts versus signal wavelength, showing the phase-matching bandwidth of the type-II SPDC waveguide. (b) Corresponding normalized single-photon count spectra for the signal channel, illustrating the spectral shape and symmetry of the generated photons. . . . .	77

4.1	Schematic for type-II SPDC using a fiber-coupled MgO:ppLN waveguide, depicting (a) Pump filtering and photon detection with coincidence analysis, (b) signal–idler birefringence compensation, and (c) HOM interferometry for verifying indistinguishability. . . . .	91
4.2	(a) Measured coincidence and accidental counts as a function of pump power, plotted on a log–log scale with corresponding linear fits indicating the slopes. (b) Measured signal–idler cross-correlation $g_{si}^{(2)}$ as a function of pump power, indicating the reduction in correlation with increasing pump power. . . . .	92
4.3	Impact of quantum efficiency at fixed $\tau_d = 5 \mu s$ and $\tau_{bw} = 128 ps$ on (a) Signal counts (b) Coincidence counts, (c) Accidental coincidences, and (d) $g_{si}^2(0)$ , scaled with pump power. Insets display the theoretical prediction of the respective curves as a function of pump power. . . . .	93
4.4	Impact of dead time at fixed $\eta = 35\%$ and $\tau_{bw} = 128 ps$ , on (a) Signal counts (b) Coincidence counts, (c) Accidental coincidences, and (d) $g_{si}^2(0)$ , as a function of pump power. Insets show the theoretical prediction of the respective curves as a function of pump power. . . . .	96
4.5	Demonstrating the effects of bin width at fixed $\eta = 35\%$ and $\tau_d = 10 \mu s$ (without birefringence compensation) on (a) Coincidence count rate, (b) Accidental coincidence rate, and (c) $g_{si}^2(0)$ , as a function of pump power; Insets in (c) depicts $g_{si}^2(0)$ as a function of bin width at $25 \mu W$ pump power. . . . .	97
4.6	Demonstrating the effects of bin width at fixed $\eta = 35\%$ and $\tau_d = 10 \mu s$ (post birefringence compensation) on (d) Coincidence count rate, (e) Accidental coincidence rate, and (f) $g_{si}^2(0)$ , as a function of pump power. Insets in (a), (b) and (c) shows the theoretical prediction of the respective curves as a function of pump power. Inset in (c) also depicts $g_{si}^2(0)$ as a function of bin width at $25 \mu W$ pump power. . . . .	98
4.7	HOM interferometry showing dip at $\eta = 35\%$ and $\tau_d = 10 \mu s$ for (a) $\tau_{bw} = 512 ps$ , and (b) $\tau_{bw} = 64 ps$ ; (c) Raw visibility and (d) Net visibility, as a function of pump power. . . . .	102
5.1	Experimental setup for generation of polarization entanglement through the type-II fiber-coupled MgO:ppLN waveguide, where (a) birefringence compensation between the signal and idler, pump filtering and state separation between Alice and Bob and (b) quantum tomography and state analysis. . . . .	109
5.2	Sinusoids depicting change in power in the output ports of the polarizer FPBS (see Fig. 5.1) for optimizing the polarization controllers before the polarizer setups. (a) depicts the results for V-polarized laser beam pertaining to V-polarized photons, (b) depicts the results for H-polarized laser beam pertaining to H-polarized photons. Orange curves represents port 1 of the FPBS and blue curves represents port 2 of the FPBS. . . . .	112

5.3	Two-photon interference showing bosonic (dip) and fermionic (peak) symmetry responses as a function of optical path difference $\delta$ . Markers denote experimental data, while dashed lines show theoretical fits. . . . .	113
5.4	Polarization-correlation fringes measured in the H, D, V, and A bases fixed in one arm as the HWP angle is scanned in the other arm. The sinusoidal fits illustrate high-visibility modulation across orthogonal unbiased polarization bases. . . . .	114
5.5	Quantum state tomography (QST) of the generated polarization-entangled state. Reconstructed density matrices (real and imaginary parts) for (a, b) $ \psi^-\rangle$ Bell state, and (c, d) $ \psi^+\rangle$ Bell state . . . . .	117
5.6	Long operation stability measurements of the entangled-photon source, showing the evolution of (a) visibility in H, V, D and A bases, (b)QBER and CHSH S-parameter, and (c) fidelity and concurrence, over a period of 10 h for $ \psi^+\rangle$ Bell state. . . . .	118
5.7	Effect of pump power on (a) visibility in H/D/V/A bases, (b) Variation of state fidelity and concurrence, (c) QBER and S-parameter, and (d) estimated secure key rate, with inset showing corresponding single-photon count rates. . . . .	120
6.1	Generalised Bode plots highlighting the gain ( $\omega_{gc}$ ) and phase ( $\omega_{pc}$ ) crossover frequencies and the corresponding gain and phase margins . . . . .	127
6.2	Adjustable voltage regulator for negative or positive voltages using IC-LM337 and LM317 respectively. . . . .	131
6.3	Simulated output voltages obtained from the adjustable voltage regulator in Fig. 6.2. . . . .	132
6.4	Current subtraction design of BHD showing the currents are first subtracted and then converted to voltages. Additional adjustable bias voltages and differential fine-tuning circuits enhance the performance of this design. . .	132
6.5	(a) Simulated transimpedance gain magnitude, (b) corresponding phase response across frequency for $y = 1\%, 50\%, 99\%$ in current subtraction design of BHD. . . . .	134
6.6	Transient response of the current subtraction architecture, for $y = 1\%, 50\%, 99\%$ .134	
6.7	Simulated noise amplitude spectral density of the current subtraction design as a function of frequency, with inset showing the broadband noise profile up to the MHz range in log scale. . . . .	134
6.8	Variable gain circuit design for BHD showing gain of one TIA can be altered through feedback resistor R. . . . .	135
6.9	(a) Simulated transimpedance gain magnitude, (b) corresponding phase response, across frequency for $R = 3.5\text{ k}\Omega - 5\text{ k}\Omega$ in variable gain design of BHD. . . . .	136
6.10	Transient response of the variable gain architecture. . . . .	136

6.11	Simulated noise amplitude spectral density of the variable gain design as a function of frequency, with inset showing the broadband noise profile up to the MHz range in log scale. . . . .	136
6.12	Variable gain circuitry with a differential amplifier on the output. . . . .	137
6.13	Simulated noise amplitude spectral density of the variable gain design with differential amplification, as a function of frequency, with inset showing the broadband noise profile up to the MHz range in log scale. . . . .	137
6.14	Variable gain circuit design for BHD showing gain of one TIA can be altered through feedback resistor R. . . . .	138
6.15	Experimental setup for measuring the CMRR of the balanced homodyne detector. . . . .	139
7.1	Comparison of reported squeezing levels over the years for free-space (left) and fiber-coupled (right) implementations based on telecom wavelength of 1550 nm. This shows the inclination towards and relevance of fully-guided compact sources in the past decade.[43, 60, 164–172] for free-space and [9, 58, 59, 61, 173, 174] for fiber-coupled . . . . .	143
7.2	Schematic of the apparatus used to generate and analyze squeezed states at a wavelength of 1550 nm. PC- Polarization controller; VOA-Variable optical attenuator, PM-Phase modulator, FBS- Fiber beam splitter; ESA-Electronic Spectrum Analyzer. . . . .	145
7.3	Balanced shot-noise spectra for different LO powers. . . . .	146
7.4	(a) Zero-span measurement of squeezing and anti-squeezing noise levels at 3.06 MHz, at 310 mW pump power with spectrum analyzer resolution and the video bandwidths set to 39 kHz and 1 Hz, respectively; (b) Squeezing and anti-squeezing levels versus pump power fitted curves. Shot noise is shown for reference. . . . .	147
7.5	Purity $\mu$ and Von Neumann entropy (S) as a function of squeezing level, comparing theoretical predictions with experimental results. . . . .	152
7.6	(a) Quantum Fisher information $F_{i\phi}$ for phase-sensitivity estimation plotted as a function of the corresponding squeezing and antisqueezing levels. (b) Phase-estimation variance obtained from the QCRB and SQL. The inset highlights the quantum advantage achieved with squeezed states over coherent states for various squeezing strengths (in dB). . . . .	154
7.7	(a) Dependence of the entanglement potential (EP), and (b) Duan’s inseparability $I$ , on the detected squeezing variance (in dB), with the fitted trendlines indicating the expected variation of each metric with increasing squeezing. . . . .	156
7.8	Quantum teleportation fidelity estimation as a function of squeezing and anti-squeezing levels.[58, 59, 61, 174] . . . . .	158
1	Homodyne schematic (designed by Tomoki Isogai). . . . .	176
2	PCB layout of the balanced homodyne detection circuit. . . . .	177

# List of Tables

1.1	Projections for quantum state tomography using HWP followed by QWP at the transmission port of the PBS (in Fig. 1.10). . . . .	36
3.1	Comparison of reported type-II SPDC ppLN/W based photon-pair sources at 1540–1560 nm. . . . .	74
4.1	Comparison of signal, coincidence, and accidental counts across multiple experimental parameter settings; $A = m_1 - m_2$ , $B = m_2 - m_3$ , $C = m_3 - m_4$ . . . . .	95
5.1	Comparative summary of state-of-the-art type-II waveguide entangled photon-pair sources at telecom wavelengths. . . . .	121
7.1	Benchmarking squeezing metrics across integrated and guided-wave single-mode squeezed light sources at telecom wavelengths. . . . .	160

# Abbreviations

<b>DV</b>	<b>Discrete Variable</b>
<b>CV</b>	<b>Continuous Variable</b>
<b>SPDC</b>	<b>Spontaneous Parametric Down-Conversion</b>
<b>SFWM</b>	<b>Spontaneous Four-Wave Mixing</b>
<b>NV</b>	<b>Nitrogen-Vacancy</b>
<b>QKD</b>	<b>Quantum Key Distribution</b>
<b>CV-QKD</b>	<b>Continuous Variable Quantum Key Distribution</b>
<b>SHG</b>	<b>Second Harmonic Generation</b>
<b>ppLN</b>	<b>Periodically Poled Lithium Niobate</b>
<b>MgO:ppLN</b>	<b>Magnesium-Oxide Periodically Poled Lithium Niobate</b>
<b>LNOI</b>	<b>Lithium Niobate On Insulator</b>
<b>JSI</b>	<b>Joint Spectral Intensity</b>
<b>JSA</b>	<b>Joint Spectral Amplitude</b>
<b>CAR</b>	<b>Coincidence-To-Accidental Ratio</b>
<b>CSR</b>	<b>Coincidence-To-Signal Ratio</b>
<b>HOM</b>	<b>Hong-Ou-Mandel</b>
<b>QBER</b>	<b>Quantum Bit Error Rate</b>
<b>CHSH</b>	<b>Clauser-Horne-Shimony-Holt</b>
<b>QFI</b>	<b>Quantum Fisher Information</b>
<b>QST</b>	<b>Quantum State Tomography</b>
<b>PC</b>	<b>Polarization Controller</b>
<b>PBS</b>	<b>Polarizing Beam Splitter</b>
<b>FPBS</b>	<b>Fiber Polarization Beam Splitter</b>
<b>IOF</b>	<b>Inline Optical Filter</b>
<b>DTF</b>	<b>Digital Tunable Filter</b>
<b>PMT</b>	<b>Phase Matching Temperature</b>

## *Abbreviations*

---

<b>SPD</b>	<b>Single Photon Detector</b>
<b>SNSPD</b>	<b>Superconducting Nanowire Single-Photon Detector</b>
<b>APD</b>	<b>Avalanche Photodiode</b>
<b>TDC</b>	<b>Time-To-Digital Converter</b>
<b>LO</b>	<b>Local Oscillator</b>
<b>RF</b>	<b>Radio Frequency</b>
<b>DC</b>	<b>Direct Current</b>
<b>AC</b>	<b>Alternating Current</b>
<b>BHD</b>	<b>Balanced Homodyne Detection</b>
<b>TIA</b>	<b>TransImpedance Amplifier</b>
<b>ABV</b>	<b>Adjustable Bias Voltage</b>
<b>FFT</b>	<b>Fast Fourier Transform</b>
<b>SMF</b>	<b>Single Mode Fiber</b>
<b>MMF</b>	<b>Multi Mode Fiber</b>
<b>WDM</b>	<b>Wavelength Division Multiplexing</b>
<b>DWDM</b>	<b>Dense Wavelength Division Multiplexing</b>
<b>ITU</b>	<b>International Telecommunication Union</b>
<b>PMD</b>	<b>Polarization Mode Dispersion</b>
<b>PDL</b>	<b>Polarization Dependent Loss</b>
<b>ODL</b>	<b>Optical Delay Line</b>
<b>DDL</b>	<b>Differential Delay Line</b>
<b>SNR</b>	<b>Signal-To-Noise Ratio</b>
<b>ESA</b>	<b>Electronic Spectrum Analyzer</b>

# Symbols

$c$	speed of light in vacuum
$\epsilon$	permittivity / dielectric constant
$\epsilon_0$	vacuum permittivity
$\mu_0$	vacuum permeability
$\chi^{(1)}$	linear susceptibility
$\chi^{(2)}$	second-order nonlinear susceptibility
$k$	wavevector
$k_0$	free-space wavevector
$k_p, k_s, k_i$	pump, signal, idler wavevectors
$n$	refractive index
$n_{\text{eff}}$	effective refractive index
$n_r$	reference refractive index
$\omega$	angular frequency
$\omega_p, \omega_s, \omega_i$	pump, signal, idler frequencies
$\lambda$	wavelength
$\lambda_p, \lambda_s, \lambda_i$	pump, signal, idler wavelengths
$\Delta k$	phase mismatch
$\Delta\omega$	frequency detuning
$\Delta\lambda$	spectral bandwidth
$\tau$	temporal delay
$\Delta\tau$	temporal walk-off
$\eta$	efficiency (detection / conversion)
$\Gamma$	nonlinear overlap factor
$\Phi$	biphoton amplitude
$g_{si}^{(2)}(0)$	zero-delay cross-correlation
$S$	CHSH Bell parameter+Von Neumann entropy

$F$	quantum-state fidelity
$C$	concurrence
$V$	interference visibility
$K$	Schmidt number
$P$	pump power / polarization
$E$	electric field
$B$	magnetic field
$D$	electric displacement field
$J$	current density
$a, a^\dagger$	annihilation and creation operators
$E^{(+)}, E^{(-)}$	positive/negative frequency field operators
$H_{\text{int}}$	interaction Hamiltonian
$\rho$	density matrix
$P(\theta_1, \theta_2)$	projection probability
$l$	orbital angular momentum index
$r$	radial mode index
$\phi$	azimuthal angle
$z$	propagation distance
$o, e$	ordinary and extraordinary photons
$\Lambda$	poling period
$L$	crystal length
$S_\lambda$	spectral brightness
$S_B$	source brightness
$N_{\text{error}}$	erroneous coincidence counts
$N_{\text{total}}$	total coincidence counts
$\mu$	state purity
$\nu$	symplectic eigenvalue
$r$	squeezing parameter
$S(\omega)$	noise spectrum
$S_x, S_p$	quadrature noise spectra
$V_x, V_p$	quadrature variances
$\hat{x}, \hat{p}$	quadrature operators
$\xi$	loss factor
$T, R$	transmission and reflection coefficients
$\bar{n}$	mean photon number

## *Symbols*

---

$\theta$	measurement phase
$\delta\phi$	phase estimation error
$\phi_{\text{LO}}$	local oscillator phase
$M$	number of measurements
$\sigma$	standard deviation
$\sigma_{\text{el}}$	electronic noise
$\sigma_{\text{shot}}$	shot noise
$I_{\text{sig}}$	signal photocurrent
$I_{\text{diff}}$	difference photocurrent
$G$	gain (electronic)
$\tau_d$	detector dead time
$\tau_c$	coincidence window
$R_{\text{dc}}$	dark-count rate
$\eta_{\text{det}}$	detector quantum efficiency
$\eta_{\text{fiber}}$	fiber coupling efficiency
$\eta_{\text{sys}}$	total system efficiency